Is fluorine incorporation in the La0.6Sr0.4Co0.2Fe0.8O3–δ improving its electrochemical behavior for Solid Oxide Cells applications?

Zonghao Shen, Jean-Marc. Bassat, Sébastien Fourcade, Alain Demourgues, Etienne Durand, Lionel Teule-gay, Mathieu Duttine, Jacinthe Gamon

ADVANCED ENERGY MATERIALS
www.advenergymat.de

Is Fluorine Incorporation in the $La_{0.6}Sr_{0.4}Co_{0.2}Fe_{0.8}O_{3-\delta}$ Improving Its Electrochemical Behavior for Solid Oxide Cells Applications?

Zonghao Shen, Jean-Marc Bassat, Sebastien Fourcade, Alain Demourgues, Etienne Durand, Lionel Teule-Gay, Mathieu Duttine, and Jacinthe Gamon**

F-doped $La_{0.6}Sr_{0.4}Co_{0.2}Fe_{0.8}O_{3-x-\delta}F_x$ (LSCFF*x*, $x = 0.05$, 0.10, and 0.20) materials are evaluated as oxygen electrodes for solid oxide fuel and electrolyser cell application. Materials have been prepared via low-temperature topotactic route by fluorination of the parent oxide with polyvinylidene fluorine (PVDF). A decrease in the polarisation resistance (R_p) is observed for the "LSCFF*x*" symmetric cells. However, the improved electrochemical behavior for the symmetric cells cannot be explained by the presence of fluorine, as post mortem chemical analysis shows that fluorine is absent from the materials after the calcination treatment, contradicting previous results from the literature and calling for deeper understanding. The presence of fluorine is proved to result in a sluggish surface exchange rate compared with the LSCF oxide via pulsed isotopic exchange technique. Despite the absence of fluorine in the fabricated symmetric cell, annealing with PVDF at low temperatures prior to the electrode fabrication is proven to be a beneficial step to improve the electrochemical performance of LSCF material with applications for solid oxide cells. Studies with room temperature X-ray diffraction, X-ray photoelectron spectroscopy, and Mössbauer spectroscopy suggest that increased oxygen vacancy concentration, structural disorder and changes in the cobalt/iron valence state distribution are potential explanations for the reduced R_p.

1. Introduction

With the increased demand for sustainable green energy, hydrogen energy plays an indispensable role in realising net-zero.[1] Among hydrogen technologies, solid oxide cells (SOCs) are of particular interest as these ceramic cells are able to operate in two different modes: the solid oxide electrolyser cell mode (SOEC) where the electrical power is converted to gas, e.g., by electrolysing water to produce hydrogen, and the solid oxide fuel cell (SOFC) mode where the energy is produced from the fuel gas such as H_2 with water as the only by-product. A typical SOC comprises multiple ceramic layers and the three main components are fuel electrode, electrolyte and oxygen electrode. Among all these components, the oxygen electrode contributes significantly to the resistance and degradation.[2] Traditional oxygen electrode materials are lanthanum-based oxide perovskites e.g. $(La,Sr)(Co,Fe)O_{3-\delta}$, $(La,Sr)MnO_{3-\delta}$ (LSM), or composites with Yttria stabilized Zirconia (YSZ) or gadolinium-doped ceria (CGO), etc. Recently interests are also growing in other materials such as Ruddlesden–Popper nickelate oxides, $Ln_{n+1}Ni_nO_{3n+1+\delta}$ (Ln = La, Pr, Nd, n = 1,2,3...). To efficiently function in SOCs, the oxygen electrode is required to meet certain criteria. Some principal ones are sufficient electronic and ionic conductivity, fast oxygen reduction reaction (ORR) and oxygen evolution reaction (OER) as well as compatible thermal expansion coefficients to the common electrolytes. Thus, in order to tune the properties of the oxide materials, different optimisation strategies have been applied. A common approach consists in substituting different elements in the cation sublattice, a method which has been widely reported in the literature.

In addition to cation substitution, tuning the anionic sublattice with hydrogen, nitrogen, fluorine, chlorine etc. appears as an original and efficient strategy for modulating properties of functional materials and raises growing interest.[3] Among these elements, with respect to applications for solid oxide cells or oxygen transport membranes (OTMs), fluorine is of particular interest as it has a similar ionic radius ($r_{F^-} = 1.36$Å) as oxygen ions ($r_{O^{2-}} = 1.40$ Å)[4] and it is therefore able to occupy the

Z. Shen, J.-M. Bassat, S. Fourcade, A. Demourgues, E. Durand, L. Teule-Gay, M. Duttine, J. Gamon
Univ. Bordeaux
France University
CNRS
Bordeaux INP
ICMCB
UMR 5026, Pessac F-33600, France
E-mail: zonghao.shen@grenoble-inp.fr; jacinthe.gamon@icmcb.cnrs.fr
Z. Shen
Grenoble Alpes
CNRS
Grenoble-INP
LMGP
Grenoble 38000, France
The ORCID identification number(s) for the author(s) of this article can be found under https://doi.org/10.1002/aenm.202401518

DOI: 10.1002/aenm.202401518

oxygen site in the lattice, bringing anionic disorder, favourable for oxygen mobility.[5] Moreover, the strong electronegativity of fluorine is predicted to destabilise the metal-oxygen bond, which is suggested to be beneficial for increasing the oxygen diffusion kinetics.[6,7] Also, with F incorporation, the lower electronic charge of the foreign anions is expected to result in the concomitant reduction of the cation oxidation state in order to maintain electronic neutrality, which modulates electronic transport properties.

To introduce F into the oxide lattice, different fluorination agents have been reported in the literature, such as NH_4F,[8–10] MF_2 (M is the metal element in the desired materials, e.g. SrF_2, CaF_2 etc.),[9,11–14] XeF_2,[15] F_2 gas.[16] However, these methods may introduce undesirable impurities, uncontrollable fluorination levels or/and toxic and difficult handling processes. In 2002, Slater[17] has reported a low-temperature fluorination method with solid poly(vinylidene fluoride) (PVDF) binder to achieve high-quality samples. This route is facile, safe and more controllable with the amount of incorporated fluorine, and it has been applied to successfully introduce fluorine in a variety of different materials, for instance $La_2NiO_{2.5}F_3$,[18] $La_{1-x}Sr_xFeO_{3-x}F_x$,[19] $La_{1-x}Sr_xFe_{1-y}Co_yO_{3-\delta}$,[20] $Sr_xBa_{1-x}FeO_2F$.[21]

Since recent decade, high-profile papers on different oxide materials have reported that a small amount of F incorporation is capable of improving the electrochemical and oxygen transport performance of materials applied in high-temperature devices such as OTMs and SOCs.[6,13,22–25] For example, $SrCo_{0.9}Nb_{0.1}O_{3-\delta}F_{0.1}$[12] has presented a two times higher oxygen permeation rate at 600 °C compared with its parent oxide material. A near 40% drop in area-specific resistance (ASR) at 600 °C for F-dopped $Pr_2NiO_{3.9+\delta}F_{0.1}$ was observed compared to the $Pr_2NiO_{4+\delta}$ oxide,[10] and an analogous behavior has also been reported to F-doped $SrFeO_{3-\delta}$.[6] Despite these promising results, considering that the material preparation and device operation are both at high temperatures, the thermal stability of the oxyfluorides could potentially hinder their practical application in these high-temperature solid-state devices. Furthermore, post mortem chemical analysis on the materials to verify whether or/and the amount of F stays in the oxygen sublattice after high-temperature annealing, is even scarcely reported, or results are unconvincing, thereby questioning whether F is indeed maintained in the oxide lattice, rather than in the form of impurity.

A good thermal stability of the oxyfluoride materials means that the material has a low tendency to lose F and to decompose at elevated temperatures under an annealed atmosphere. Through thermodynamic analysis, Jacob and Saji[26] have indicated a good stability of oxyfluoride materials in an oxygen atmosphere while with the presence of water vapour, the oxyfluoride phase can lose fluorine at high temperature due to the higher thermal stability of HF compared with water molecules. Experimentally a consensus has yet to be reached and it seems to be highly material-, structural- and experimental conditions-dependent. Zhu et al.[12] have reported good thermal stability of $SrCo_{0.9}Nb_{0.1}O_{3-\delta}F_{0.1}$ (SCNF) up to 1100 °C in N_2 atmosphere via thermogravimetry analysis coupled mass spectrometry (TGA-MS), while the followed F-related species were not detailed. Similarly, Zhang et al.[6] have declared the good stability of $SrFe(O,F)_{3-\delta}$ under Ar atmosphere up to 1000 °C where only F_2 was followed. Unfortunately, no post mortem chemical analysis was reported in these articles, nor was the effect of air atmosphere screened where the high-temperature calcination took place. Good thermal stability of fluorinated-hexagonal perovskite $BaFe(O,F)_{3-\delta}$ up to 1000 °C in air has been demonstrated by Sturza et al.[27] while Clemens et al.[21] have revealed that the cubic perovskite-structured $(Ba,Sr)Fe(O,F)_{3-\delta}$ has suffered decomposition yielding $(Ba/Sr)F_2$ salts at 750 °C. Moreover, the decomposition of the Ruddlesden–Popper (RP) phase $La_2NiO_{2.5}F_3$ in the regime of 400–450 °C, $La_2Cu_{0.8}Ni_{0.2}O_3F_2$ at 530 °C and $La_2CuO_3F_2$ at 400 °C with LaF_3/LaOF as the impurities was reported by Jacobs et al.[18,28] A recent work by Osinkin et al.[29] has confirmed that fluorine has escaped from the anion sublattice of the cubic perovskite $Sr_{1.95}Fe_{1.4}Ni_{0.1}Mo_{0.5}(O,F)_{6-\delta}$ after annealing at 1100 °C despite an improved electrochemical behavior was still observed with the absence of fluorine. Therefore, it appears challenging to answer the questions regarding the fluorine incorporation and its effects in light of the incomprehensive chemical analysis on some reported materials: whether fluorine is indeed doped in the oxide lattice, whether the amount of the incorporated F after heat treatment is the same as the nominated starting value and whether the improved behavior is undoubtedly direct from the presence of F.

In this work, our goal is to tackle these interrogations by investigating the structure, performance and stability of a fluorine-doped state-of-art mixed electronic and ionic conducting (MIEC) material $La_{0.6}Sr_{0.4}Co_{0.2}Fe_{0.8}O_{3-\delta}$ (LSCF6428) as the oxygen electrode in SOCs. The F-doped $La_{0.6}Sr_{0.4}Co_{0.2}Fe_{0.8}O_{3-x-\delta}F_x$ powders (LSCFFx, x = 0.05, 0.10, and 0.20) were obtained via low temperature fluorination reaction with PVDF binder at 400 °C. The incorporation of F in the oxide lattice has been carefully studied by X-ray diffraction (XRD), and X-ray photoelectron spectroscopy (XPS) and the F composition was further quantified with a fluoride selective electrode. Symmetric cells were then prepared with both LSCF and LSCFFx materials, and the cells performance was characterised using electrochemical impedance spectroscopy. Furthermore, the thermal stability of the LSCFFx oxyfluoride was discussed with the help of in situ TGA-MS measurements. A comprehensive post mortem chemical and structural analysis has been carried out after heat treatment up to 950 °C combining F-selective electrode, XRD, XPS Mössbauer spectroscopy and time-of-flight secondary ion mass spectrometry (ToF-SIMS) measurements. The effect of F-doping in the LSCFFx materials on oxygen surface exchange dynamics has also been studied with the pulsed isotopic exchange (PIE) technique where the F-incorporation was verified.

2. Results and Discussion

2.1. F-Incorporation in the LSCF Oxides

A small amount of La_2O_3 and $SrCO_3$ impurities has been observed for the commercially available precursor $La_{0.6}Sr_{0.4}Co_{0.2}Fe_{0.8}O_{3-\delta}$, LSCF (Figure S2, Supporting Information) oxide powders. After calcination at 850 °C for 3 hours under lab air, no trace of the secondary phase has been further detected with lab X-ray diffraction, i.e., the starting LSCF oxide after calcination is thus considered as single-phase oxide material (Figure S2, Supporting Information). The chemical composition of the LSCF oxide powders was determined with

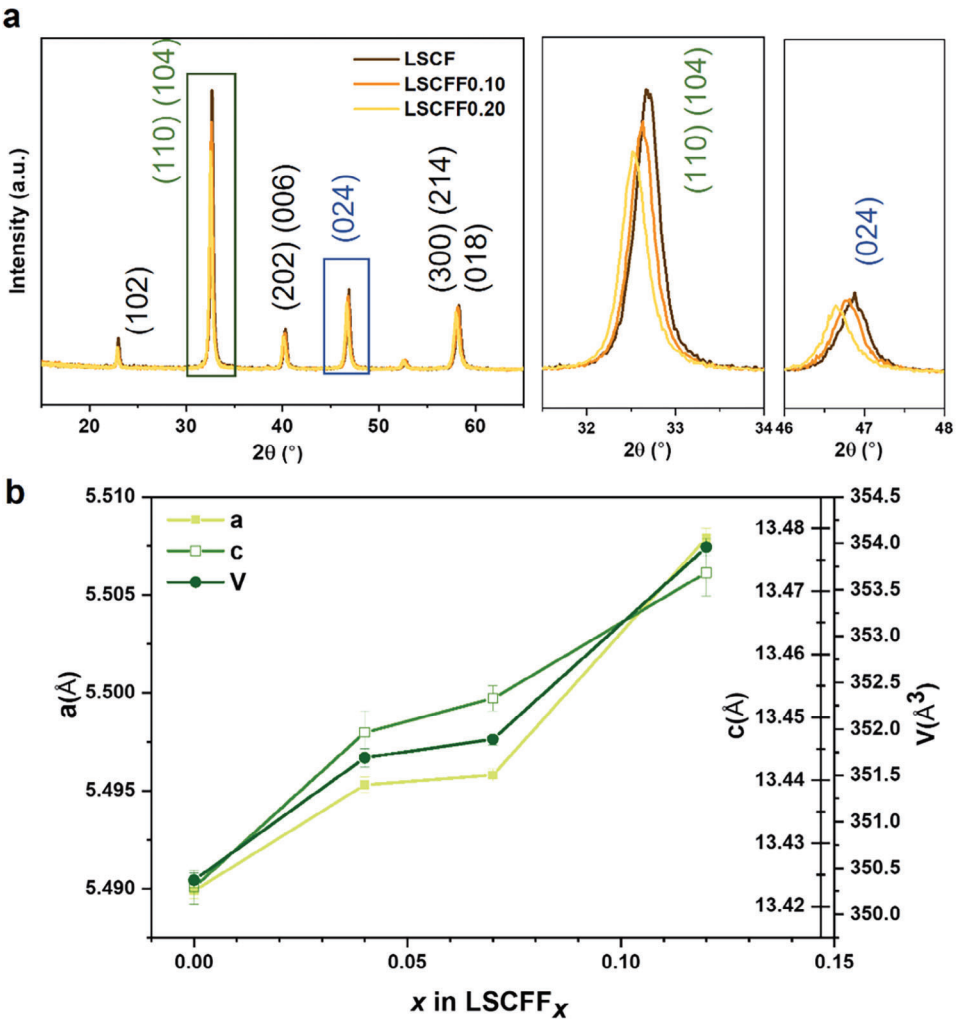

Figure 1. a) XRD patterns of the as-prepared LSCF and LSCFF*x* powders; (right) Zoom-in between $2\theta = 31.5–34°$ and 46–48° showing the shifts of the index peak position (110)/(104) and (204); b) lattice parameters variation as a function of the measured F amount in the LSCF oxide lattice.

the ICP measurement (Table S1, Supporting Information) and within the measurement errors the LSCF composition has been confirmed with 3% A-site deficiency, which can then be more precisely written as $(La_{0.62}Sr_{0.38})_{0.97}Co_{0.21}Fe_{0.79}O_{3-\delta}$ (LSCF). This is also the starting material for all following experiments in this work.

F-doped $(La_{0.62}Sr_{0.38})_{0.97}Co_{0.21}Fe_{0.79}O_{3-x-\delta}F_x$ (LSCFF*x*) powders, $x = 0.05$ (LSCFF0.05), 0.10 (LSCFF0.10), and 0.20 (LSCFF0.20) were obtained via low-temperature fluorination annealing of the stochiometric mixture of the precursor LSCF oxide and the PVDF binder. To be noted here, in this article the nominated F concentration is the F amount from the PVDF binder before the fluorination annealing. More detailed studies on the exact incorporated F amount in the LSCF anion sub-lattice after annealing will be provided later in this session. The XRD patterns of the LSCF and LSCFF*x* powders are compared in **Figure** 1a and the adjacent figures on the right zoom in the $2\theta = 31.5–34°$ and 46–48° regions for better observation on the diffraction peaks. After fluorination, all the obtained materials were confirmed as perovskite-structured single phase, same as the undoped LSCF oxide. Additionally, it is also clear that the diffraction peaks gradually shift to lower angles with higher F incorporation indicating an expansion of the lattice. Meanwhile, no obvious lattice disorder or reduced symmetry was observed until the highest F-doping amount here studied, i.e. LSCFF0.20, within the resolution of the lab X-ray. Le Bail refinement was further applied to determine the lattice parameters (Figure S3, Supporting Information) for the LSCFF*x* materials with a rhombohedral space group of $R\bar{3}c$ in all cases. It is confirmed that with F doping, the lattice parameters increase (Figure 1b; Table S2, Supporting Information) compared with the LSCF oxide, while the volume change is less significant between the samples LSCFF0.05 and LSCFF0.10.

According to previous studies, the effects of F incorporation on the oxide lattice are not consensual and seemingly depend on the materials and synthesis conditions: an expansion of lattice was reported for some F-incorporated phases in literature, such as $Sr_2TiO_3F_2$,[17] $Cu_2CuO_2F_2$,[17] $La_2NiO_3F_2$,[30] $La_{1-x}Sr_xFeO_{3-x}F_x$[19] etc., while some other ones have been reported with a decrease of lattice parameter after F incorporation, e.g. $SrCo_{0.9}Nb_{0.1}O_{3-\delta}F_{0.1}$(SCNF),[12] $Pr_2NiO_{3.9+\delta}F_{0.1}$[10] or

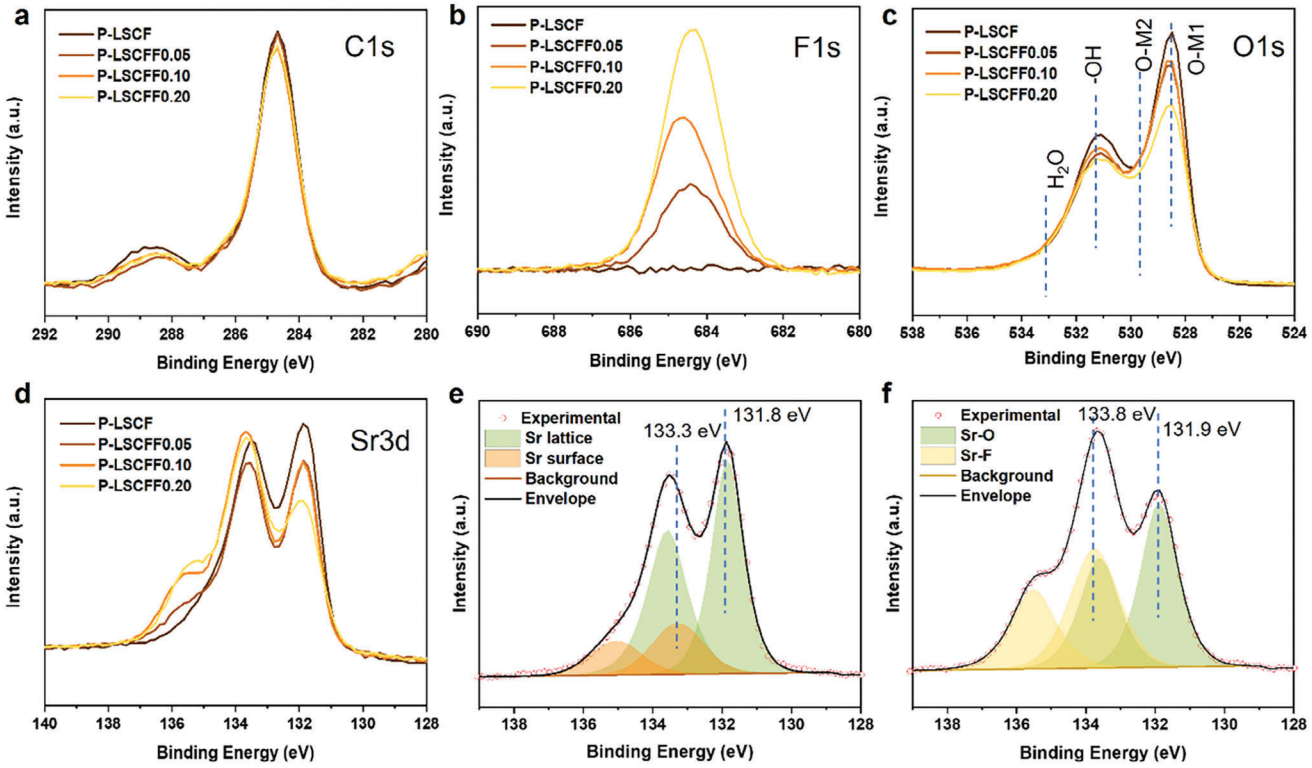

Figure 2. a–d) XPS spectra of the LSCF and as-prepared LSCFF*x* powders: C1s, F 1s, O 1s and Sr 3d, respectively. Deconvolution of the XPS Sr 3d spectra of the e) LSCF oxide and f) LSCFF0.20 oxyfluoride materials.

with unnoticeable change, such as $Nd_{1.9}Ba_{0.1}NiO_{4+\delta}F_{\gamma}$ (γ = 0, 0.03, 0.05, 0.07, and 0.1).[13] Additionally, a contradicting behavior has also been reported for the oxide with the same chemical composition in different studies, for instance for the material with the formula of $Ba_{0.5}Sr_{0.5}Co_{0.2}Fe_{0.8}O_{3-\delta}$ (BSCF) Zhu et al. then Xie et al.[12,31] have observed a decrease in the lattice parameters with F incorporation, while Xiong et al.[32] has reported a slightly expanded lattice. The potential reason for this contradictory behavior could result from the competition between the substitution of oxygen ion by fluorine ion with relatively smaller radius (leading to a reduction of the overall metal oxidation states), and insertion of fluorine ion in available vacant sites of the structure (leading to an increase of the overall metal oxidation state). This competition between substitution and incorporation could be the reason for the deviation from the linear behavior observed in Figure 1b, with a plateau for intermediate *x* values.

For the perovskite-structured, $(La,Sr)(Co,Fe)O_{3-\delta}$ compounds, an expansion of the lattice has been clearly observed by X-ray absorption and Mössbauer spectroscopy measurements by Berry et al.,[20] due to the consequently reduced oxidation state of the transition metals in the oxides after F incorporation, with high amounts of F doping (synthesis performed with 1:0.75 M ratio (precursor oxide: CH_2CF_2 monomer unit)). Nevertheless, Liu et al.[33] have claimed an opposite trend for F-doped LSCFF materials. But after carefully revisiting their XRD patterns, it can be confirmed that with the increased F doping the Bragg diffraction peaks present negative shifts, i.e., towards lower 2θ, suggesting an expansion of the lattice, then in agreement with Berry et al.[20] and this work. Thus, it can be concluded that a F doping in the LSCF oxide results in a lattice expansion which is mainly associated with the reduced oxidation states of the transition metals, as expected.

The presence and incorporation of fluorine in the LSCF anion sublattice was further investigated by X-ray photoelectron spectroscopy (XPS) measurements. All the XPS results are aligned to C1s core level (284.8 eV) and the applied measuring conditions of XPS on all LSCFF*x* samples are identical. **Figure** 2a–d presents a comparison of XPS spectra of C 1s, F 1s, O 1s, and Sr 3d core level respectively for each LSCFF*x* sample. The spectra of C 1s, La 3d, Co 2p, and Fe 2p, are plotted in the supplementary information Figure S4a–d (Supporting Information) and the details of the deconvolution of Sr 3d XPS spectra for all samples are listed in Table S3 (Supporting Information).

In Figure 2b, the F peak locates at ca. 684.4 eV which falls in the characteristic range for metal fluoride[34] verifying the presence of fluorine. Moreover, the peak intensity of F 1s core level increases with increased F doping and it is also confirmed that no F is observed for the LSCF oxide within the detection limit of XPS. A ratio of F concentration $C_{LSCFF0.05}$:$C_{LSCFF0.10}$:$C_{LSCFF0.20}$ = 1.0:1.8:2.9 in the LSCFF*x* materials is determined according to the area under the F 1s peaks which, albeit follows the trend, varies from its nominated ratios, i.e. $C_{LSCFF0.05}$: $C_{LSCFF0.10}$:$C_{LSCFF0.20}$ = 1.0:2.0:4.0. Considering XPS spectra only provides the surface chemical information within a few nanometers, depth profiling with Ar^+ sputtering beam was further performed on all powder samples. Figure

S4e,f (Supporting Information) presents the F 1s spectra of the LSCF oxide and LSCFF0.20 oxyfluoride samples following the Ar^+ sputtering step. It is shown that except for the binding energy shift which was induced by the Ar^+ milling, no noticeable changes occur regarding the depth profiling analysis described above. Moreover, in order to determine the actual F concentration in the oxyfluoride samples, chemical analysis using a fluoride ion selective electrode was carried out on the LSCFF0.20 sample. This quantitative measurement indicates that the actual F concentration in the LSCFF0.20 sample is close to 0.12(1), meaning that during the thermal annealing at 400 °C only ≈ 60% of the F in the PVDF binder has been incorporated in the LSCFF0.20 sample. Combining the results obtained with the F ion selective electrode, ICP measurements as well as the XPS F 1s spectra, the chemical composition for the expected LSCFF0.05, LSCFF0.10 and LSCFF0.20 materials can be written, more precisely, as $(La_{0.62}Sr_{0.38})_{0.97}Co_{0.21}Fe_{0.79}O_{2.96-\delta}F_{0.040(3)}$, $(La_{0.62}Sr_{0.38})_{0.97}Co_{0.21}Fe_{0.79}O_{2.93-\delta}F_{0.070(5)}$, and $(La_{0.62}Sr_{0.38})_{0.97}Co_{0.21}Fe_{0.79}O_{2.88-\delta}F_{0.12(1)}$, respectively. In this article, to avoid confusion and to be simplified, the abbreviation form of LSCFF0.05, 0.10, and 0.20 will still however be kept.

The O 1s spectra are shown in Figure 2c where peaks located at the lower binding energies, ca. 528.4 and 529.5 eV are attributed to O-metal bonds in the crystal network[35] and the others located at higher binding energies, 531.2 and 533.3 eV arise from surface hydroxyls and the irreversibly adsorbed molecular water.[36] The detailed deconvolution for O 1s core level of the LSCF and LSCFF0.20 is provided in Figure S4g,h (Supporting Information). According to Figure 2c, it is clear that with the increased F incorporation, on the contrary to F 1s spectra, a decreased intensity of the O-Metal binding can be observed, as expected.

Focussing on the Sr 3d core level (Figure 2d), for all the analysed samples two sets of spin-orbit split doublets are evidenced; a detailed deconvolution obtained for the LSCF oxide and LSCFF0.20 oxyfluoride are presented in Figure 2e,f, respectively. One doublet located at lower binding energy, ca. 131.9 eV for both spectra can be attributed to the Sr—O bond in the bulk of the material.[37,38] On the contrary, the other doublet presents different binding energies for the LSCF oxide and LSCFF oxyfluoride materials. For the LSCF oxide, the doublet is attributed as Sr surface-bound, $Sr(OH)_2$, SrO_x (133.3 eV).[37,38] For the LSCFF samples, the doublet is located at higher binding energy (133.8 eV), which agrees well with the reference sample SrF_2 and could therefore be attributed to the Sr—F bond. Moreover, with higher F doping, the intensity of this Sr-F doublet increases correspondingly. This suggests that fluorine anions are preferentially coordinated to Sr^{2+} rather than La^{3+} cations.

Finally, the XPS spectra of O1s and Sr 3d, together with the XRD analysis where an increase of the cell volume and the absence of crystalline F containing impurities have been confirmed, point towards the incorporation of F in the anion sublattice of LSCF oxide by partially substituting O^{2-} in the form of F^- and bonding with Sr cation. On the contrary to the spectra of F 1s, O 1s and Sr 3d which present obviously different behavior for different LSCFF*x* materials, for other elements in the LSCFF*x* materials, the XPS spectra of La 3d, Co 2p, and Fe 2p core levels, Figure S4b–d (Supporting Information), only present subtle differences with the increased fluorination level under the measurement limitation of XPS. Thus, the influence of F-incorporation on the La 3d, Co 2p, and Fe 2p core levels will not be further discussed in this article.

2.2. Cell Performance

Symmetric cells LSCF(F*x*)/CGO/YSZ/CGO/LSCF(F*x*) were fabricated, to study the effects of F incorporation in LSCF and their potential application as oxygen electrodes in SOCs. In order to mitigate the influence of external parameters such as added interlayer, and microstructure of the electrodes such as particle morphology, porosity, and tortuosity, all the slurry recipes and the preparation procedures of the symmetric cells are kept consistently with extra care, only except the applied active electrode materials. **Figure 3**a,c are the scanning electron microscopy (SEM) images of the cross sections of the screen-printed cells after sintering, LSCF and LSCFF0.20 respectively, and Figure 3b,d are zoom-in images of each electrode presenting clearer microstructures. It is clear that the thickness of the CGO interlayer is ca. 2–3 µm while the thickness of the electrodes is ca. 17–18 µm. According to the SEM images, it is plausible to suggest that the microstructure of the screen-printed layers, such as thickness, particle sizes, tortuosity and porosity, are not the dominant factors contributing to the performance variations among this set of cells. Thus, based upon the Alder–Lane–Steele model[39] for estimation of the polarisation resistance (R_p) (Equation S8, Supporting Information), the measured electrode polarisation resistance difference can be directly linked with the different electronic and ionic conducting behavior of the electrode materials.

The electrochemical performance of the four symmetric cells (one example photo presented in Figure S5, Supporting Information insert photo) was measured with AC impedance spectroscopy. Prior to further data analysis, the data quality for each measurement was checked with the Kramer–Kronig (K–K) validity test with *Lin-KK* tool.[40] The EIS data for all cells at each temperature with K–K tests are in similar shape, an example is presented in Figure S5 (Supporting Information). The relative residuals for both the imaginary and real components are below 1% which indicates the good quality of the obtained impedance data. In the EIS figures presented below, the ohmic and inductive parts are not included, and only the polarization resistance is compared (an example of raw EIS spectra is presented in Figure S6f, Supporting Information). The Nyquist plots for each LSCFF*x*/CGO/YSZ symmetric cells at 700 and 500 °C, subtracted from the series resistance and inductive part, are displayed in **Figure 4**a,b, respectively, and the measurements at the other temperatures of 800, 750, 650, 600, and 550 °C are presented in Figure S6a–e (Supporting Information). However, the presence of artefacts at high frequencies is observed which was possibly introduced by the cables and the frequency respond analyser system (Figure S6f, Supporting Information). This was also previously seen for other material systems, $La_3Ni_2O_7$ electrode with $Ce_{0.8}Sm_{0.2}O_{2-\delta}$ electrolyte,[41] LSM-YSZ electrode with YSZ electrolyte,[42] $Ln_2NiO_{4+\delta}$ with YSZ electrolyte[43] as well as infiltrated $La_2NiO_{4+\delta}$[44] on the CGO backbone. Before further analysis, according to the Nyquist plots it is visually clear that the cells with the LSCFF*x* electrodes present smaller R_p compared to the LSCF cell and the LSCFF0.10 presents the best electrochemical performance among these four samples. Moreover, with the

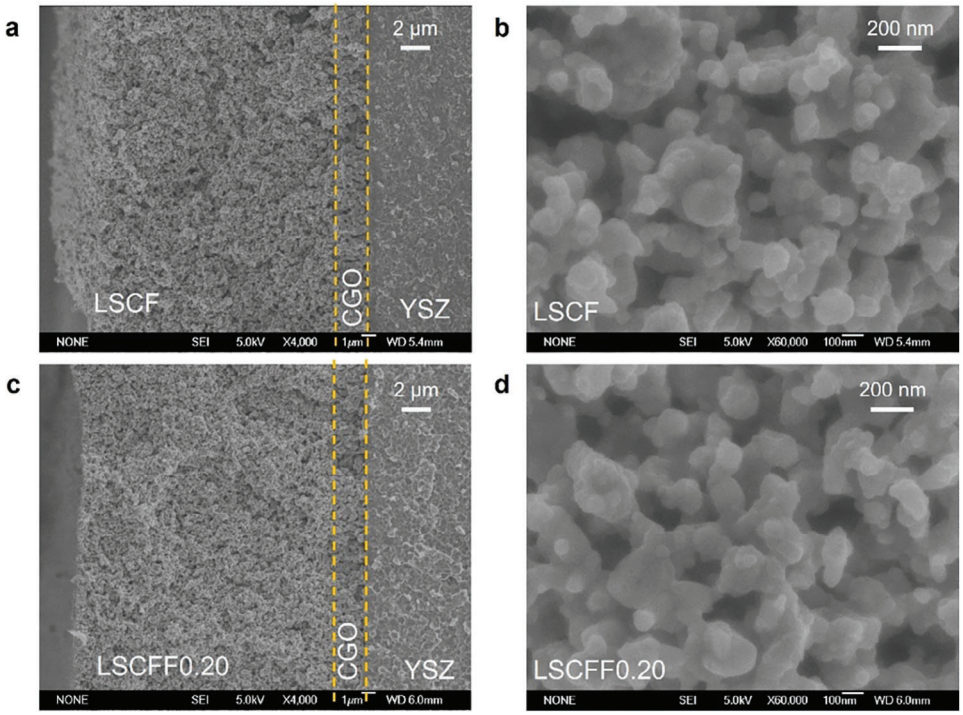

Figure 3. SEM images of the cross sections of the sintered symmetric cells a) LSCF and c) LSCFF0.20, and images b) and d) are the zoom-in images (x 60,000) on the corresponding LSCFF*x* electrode regions.

decrease in temperature, a more significant improvement in R_p can be observed while the difference among different samples at temperatures ≥ 750 °C is negligible.

The Bode plots (phase shift versus frequency) for the LSCF and LSCFF0.10 symmetric cells are presented for each measured temperature in Figure 4c,d, respectively. The Bode plots for the LSCFF0.05 and LSCFF0.20 symmetric cells are displayed in the supplementary information Figure S6g,h (Supporting Information). With the Bode plots, it is possible to identify the number of electrochemical processes, i.e. the semi-circles in a Nyquist plot. Figure 4c illustrates that at high temperatures 800-750 °C, two distinguished phases can be observed for the LSCF cell where phase P1 at high frequency is related to the charge transfer process and the low-frequency phase P2 is induced by gas diffusion.[42,43] The gas diffusion resistance is relatively stable, ~0.018-0.019 Ω, for all measured cells at varied temperatures. This also suggests the minimal influence of the microstructure on the R_p considering that all samples have similar microstructures. At high temperatures above 700 °C, the gas diffusion in the electrode plays a vital role to the total polarisation resistance and is fading away with the decrease of temperature. On the contrary to the gas diffusion resistance, it is not straightforward to evaluate the evolution of phase P1 with the decrease of temperature. It gradually increases and becomes undistinguishable due to a newly emerged third phase P3 located at medium frequencies at temperatures ≤ 700 °C. As the temperature further decreases to intermediate regions (< 650 °C), phase P3 (visible for all cells) presents a Gerischer behavior in Nyquist plot with the characteristic 45° slope at high frequency region. The R//CPE-like behavior in the low frequency region of the Gerischer element is well known as related to the bulk oxygen diffusion and oxygen surface exchange co-limiting electrode reactions for a thick MIEC electrode.[44] A similar behavior in the Bode plots is observed for all LSCFF*x* symmetric cells, LSCFF0.10 for instance in Figure 4d. Thus, the AC impedance data recorded at different temperatures were fitted with different equivalent circuit models which are displayed in each Nyquist map. To be noted here, based upon the Bode plots minimum circuit elements were added to the fitting equivalent circuit model to obtain an acceptance fitting result and meanwhile to avoid overinterpreting the physical meaning.

Furthermore, the distribution relaxation time (DRT) analysis was also performed in order to obtain a more detailed understanding of the electrochemical processes. It is clear that for all the measured LSCFF*x* samples, the DRT plots are similar in peak positions and peak area. However, differences can still be observed for the LSCF cell compared to the LSCFF*x* ones. Two examples of DRT analyses performed at 700 and 500 °C are shown in Figure 4e,f, respectively. At 700 °C, five sub-processes can be seen. Among them, the main contribution is from the peak located at far left, corresponding to the high-frequency phase P1. It can be assigned as the interface component,[45,46] i.e., the oxygen ion transfer between interfaces. Since the difference among samples is negligible and can be affected by the high-frequency inductance artefacts, we will not further comment here for phase P1. The peak at the far right, corresponding to the low-frequency phase P2, is almost identical for the four cells. This process can be attributed to the gas diffusion process in good agreement with the Bode plots. The peaks in between, in the intermediate frequency region P3, are associated with the oxygen dissociative incorporation including oxygen surface exchange and diffusion in the electrode; three sub-processes can be observed at 700 °C, namely P3H (high frequency), P3I (intermediate frequency) and P3L (low

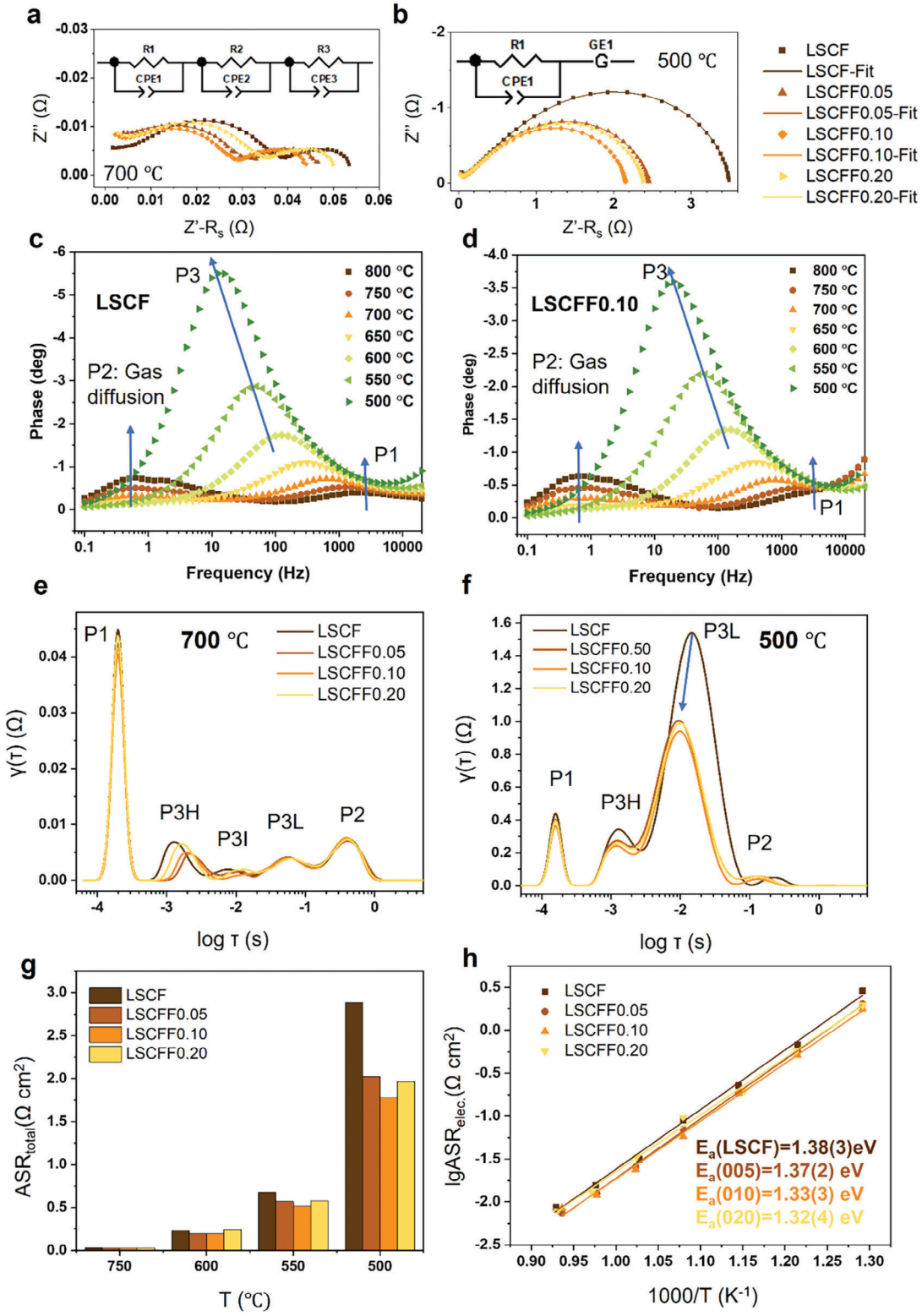

Figure 4. Electrochemical measurements and analysis on the LSCFF*x*/CGO/YSZ symmetric cells: Nyquist plots of the symmetric cells at a) 700 °C and b) 500 °C respectively; c), d) Bode plots (Phase shifts versus frequency) for the symmetric cells LSCF and LSCFF0.10 respectively at different temperatures and e), f) DRT analysis on the four symmetric cells at 700 and 500 °C; g) Total area specific resistance (ASR) of the measured symmetric cells; h) Arrhenius plots of the area specific resistance (ASR) with electrode reactions, i.e. without gas diffusion resistance, versus temperature plots for the four symmetric cells.

frequency). The main difference among the cells is from the P3H phase. At 500 °C, the dominant contribution to the resistance is generated from the P3L phase which is actually a combination of P3L+P3I since the distinguished P3I and P3L sub-processes observed at 700 °C cannot be further separated. Combining the DRT, Bode and Nyquist plot analysis, it can be deducted that the P3L (P3L+P3I) phase at 500 °C is associated with the bulk oxygen diffusion and oxygen surface exchange co-limiting electrode reactions for a thick MIEC electrode, i.e., the Gerischer behavior. Clearly, compared with the parent LSCF material, the LSCFF*x* materials present faster oxygen diffusion and/or surface exchange rate suggesting fluorination seems to be a good strategy to improve the electrochemical behavior of the oxide materials in good agreement with most literature reports.

For this set of LSCFF*x* symmetric cells, the area of the electrode is 1.65 cm^2. The area-specific resistance (ASR) can be calculated with equation ASR = R_p*A/2 where A is the area of the electrode. The comparison of ASR for different samples is presented in Figure 4g, e.g. at 600 °C the total ASR for cells with LSCF, LSCFF0.05, LSCFF0.10, and LSCFF0.20 electrodes is 0.23, 0.20, 0.19, and 0.24 Ω cm^2 respectively and at 500 °C the ASR is 2.89, 2.03, 1.78, and 1.96 Ω cm^2, respectively. Among the measured four cells, the LSCFF0.10 sample presents the best electrochemical behavior and compared with the parent LSCF material, the ASR of the LSCFF0.10 cell has been reduced by 17 % at 600 °C and 38 % at 500 °C. Additionally, the improvement in the electrochemical performance of the LSCFF cells is more significant at lower temperatures suggesting this strategy is of particular interest, especially for the intermediate temperature (IT) operating SOCs. Figure 4h presents the Arrhenius plots of the ASR only for the oxygen electrode reaction for the four samples, i.e., the resistance from gas diffusion in the electrode is excluded and the resulting activation energy presents the intrinsic material behavior. It is clear that the Arrhenius plots for all four samples present good linearity and the activation energy for the samples is very close to each other, i.e., under the experimental errors the difference is negligible.

To confirm that the improved electrochemical performance is not a fortuitous phenomenon, different sets of cells were prepared for performance optimisation. The optimisation process includes the calcination temperature of the CGO buffer layer, the thickness of the electrode layer, the receipts for the slurry etc. Albeit the polarisation resistance of different sets varies due to different electrode thickness or porosity resulting from annealing temperature, they all present similar behavior where the polarisation resistance clearly decreases for the LSCFF*x* cells compared with the untreated parent LSCF cells. Some examples of different sets of cells are presented in Figure S7 (Supporting Information) and will not be further discussed here.

Additionally, the long-term stability of the material is a key parameter for practical applications and to examine it, an ageing experiment was carried out at 700 °C for a duration of over 300 h under ambient atmosphere. A new set of symmetric cells with electrodes of LSCF and LSCFF0.20 was prepared and the evolution of R_p with ageing time for the two cells is compared in **Figure 5**a. Figure S8a,b (Supporting Information) are Nyquist plots of the LSCF and LSCFF0.20 cells respectively, for some selected annealing durations. The values of the polarisation resistance are different from Figure 4 as there are different sets of samples while among the same set, the experimental parameters were kept the same. Firstly, it again confirms the decreased R_p for the LSCFF*x* cell compared with the LSCF one. The degradation rates for LSCF and LSCFF0.20 symmetric cells are 5.7(7) % kh^{-1} (57.7 mΩ cm^2 kh^{-1}) and 4.8(2) % kh^{-1} (31.4 mΩ cm^2 kh^{-1}), respectively. The improvement in the electrochemical behavior of the LSCFFx cell does not fade away with time under the measurement conditions, which again suggests that fluorination seems to be a potentially good strategy to improve the electrochemical performance of the solid oxide cells. However, a question yet to be answered is the fluorine concentration in the oxyfluoride materials after high-temperature symmetric cell calcination and electrochemical measurement. In the following section, more detailed chemical analysis will be provided.

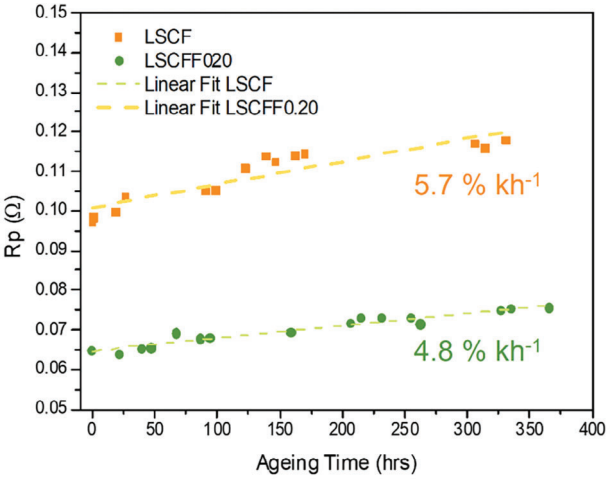

Figure 5. Ageing tests on the LSCF(F0.02)/CGO/YSZ symmetric cells (φ = 16 mm) at 700 °C under lab ambient atmosphere: polarisation resistance R_p of the measured two cells with ageing duration.

2.3. Post Mortem Analysis and Thermal Stability Studies

Albeit the improved electrochemical behavior has been reported in different oxyfluoride materials, post mortem chemical and structural analysis on the materials is rarely seen. In this work, a post mortem XRD measurement was first performed on the cells after EIS tests as presented in **Figure 6**a. Surprisingly, the observed peak shifts after the F doping (Figure 1) disappear which suggests a potential F loss for the symmetric LSCFF*x* cells after EIS. To verify the absence of F, XPS was then applied to the two symmetric cells LSCFF0.05 and LSCFF0.10 after EIS measurements (shown in Figure S9a,b, Supporting Information). The EIS results of this set of samples are presented in Figure S8c (Supporting Information). Compared with the LSCFF0.05 powders the F1s peaks for both cells are negligible and thus it confirms the fluorine loss in the symmetric cells. Additionally, considering the surface sensitivity of XPS, depth profiling with Ar^+ sputtering was further carried out to check whether more fluorine stays in the bulk of the materials. After 420 s sputtering, no obvious change of F1s peak has been detected with XPS for both samples (Figure S9c,d, Supporting Information).

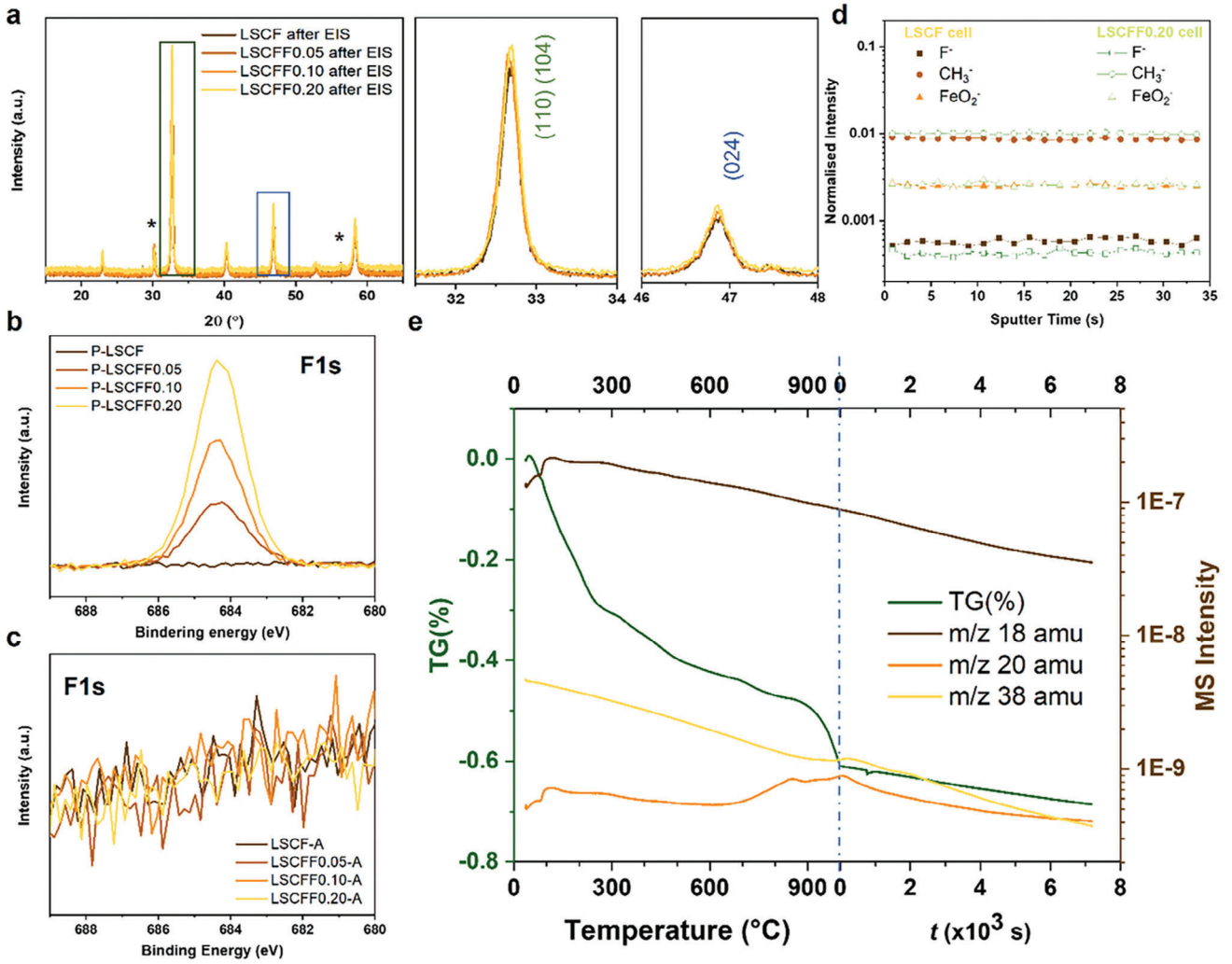

Figure 6. a) XRD patterns of the symmetric cells after EIS measurement and the adjacent image is the zoom-in between 2θ = 31.5–34° and 46–48° showing the index peak position (110)/(104) and (204) in comparison of Figure 1. The asterisk * symbol labels the diffraction peaks from the fluorite-structured CGO interlayer. b) XPS F1s spectra of the as-screen printed symmetric cells before high-temperature calcination; c) XPS F1s of the same symmetric cells after calcination at 950 °C for 4 h. d) TOF-SIMS depth profiling on the LSCF-A and LSCFF0.20-A symmetric cells after calcination at 950 °C, i.e., the same samples as Figure 6c. All the signals are normalised to the total counts. e) TGA-MS measurement of the LSCFF0.20 powders under synthetic air flow and the species with m/z = 18, 20, and 38 amu are followed by the mass spectrometer. On the left of the dashed line, the x-axis is with elevated temperature; on the right, the temperature is at 1000 °C and the x-axis is with annealing duration.

Furthermore, the next question to answer is: at which step(s) fluorine leaves the oxygen sublattice. It has been reported that fluorine doped materials, oxyfluoride, may possibly suffer from thermal stability.[26,47,48] For the LSCFF*x* symmetric cells, the F loss can happen during the symmetric cell calcination at 950 °C and/or during the EIS measurements up to 800 °C under ambient atmosphere. Moreover, after the calcination at 950 °C the amount of F left in the anion sublattice is undetermined, which further raises the question whether the improved cell performance indeed results from the F incorporation in the material. In order to have better view of the questions, here different techniques were applied for the post mortem chemical analysis and sets of ex situ and in situ measurements were also performed.

A new set of four LSCFF*x*/CGO/YSZ symmetric cells were prepared following the same protocol and the cells were all broken into halves. One half was used as the reference sample and the other half was calcined at 950 °C for 4 h (same conditions as the cells preparation for the EIS measurements). To differentiate the LSCFF*x* materials before and after calcination, in this section the materials after high temperature treatment at 950 °C are labelled as LSCFF*x*-A. Figure 6b,c present the F 1s XPS spectra before and after calcination, respectively, with alignment to C1s core level at 248.8 eV. Clearly, before 950 °C calcination the F intensity increases with the F incorporation in good agreement with the previous powder samples in Figure 2, showing that ink preparation did not alter material compositions, while after the calcination no obvious F has been detected with the detection limit of XPS. Furthermore, ToF-SIMS was also applied on the halves after calcination considering its high detection limit (ppm/ppb range), especially for fluorine thanks to its high ionisation probability,

with a Cs^+ ion beam. Considering ToF-SIMS is a half-quantitative technique due to the matrix effects; it is not possible to obtain the accurate F concentration here. However, it is obvious that the F^- signal of the LSCFF0.20-A cell is not much different from that of the LSCF-A cell (Figure 6d) and is at traces scale for both samples. Thus, based upon the XPS and TOF-SIMS results, as a major result it can be confirmed that before EIS measurements, the LSCFFx symmetric cells have already lost all of the incorporated fluorine and the improved EIS performance is unlikely directly associated with the presence of F.

In order to understand better the thermal stability of the LSCFF*x* materials, TGA-MS and F-selective electrode measurements were both performed on the LSCFF0.20 powders and the results are presented in Figure 6e and Table S4 (Supporting Information), respectively. Although some previous studies have reported good thermal stability of F-doped oxides by TGA-MS, e.g., $SrCo_{0.9}Nb_{0.1}O_{3-\delta}$,[12] $SrFeO_{3-\delta}$,[6] in these previous works only the F_2 specie with m/z = 38 was followed or the followed specie(s) were unclarified, moreover, the experiment was performed under Ar or N_2 atmospheres, then different from their calcination conditions. Some studies in the literature[26,29,47] have discussed the stability problems of the oxyfluoride materials, especially with the presence of moisture due to the thermodynamic equilibrium: indeed as HF presents higher thermodynamic stability compared with H_2O, theoretically the fluorine ions in the oxyfluoride materials have the tendency to exchange with oxygen in the H_2O molecule, resulting in the formation of HF upon heating the oxyfluoride. However, to the best of the author's knowledge, no confirmation or refutation on the formation of HF has been reported experimentally in literature,[47] while an absence of F has only been reported for the $Sr_{1.95}Fe_{1.4}Ni_{0.1}Mo_{0.5}(O,F)_{6-\delta}$ materials after annealing at 900 °C.[29]

In this work, F-related gases, F_2 and HF were both followed in the mass spectrometer during the TGA analysis, as shown in Figure 6e. An initial significant weight loss up to 200 °C is clearly observed which is mainly associated with moisture loss (m/z = 18), while a slight increase of HF is also noticed. A gradual weight loss continues at elevated temperatures up to 700 °C without noticeable changes for the F-containing gases. However, a clear increase of HF (m/z = 20) occurs at 700 °C and continues until 900 °C where a significant mass loss with a slight increase of F_2 signal (m/z = 38) is also observed. After reaching 1000 °C, the continuous weight loss is also potentially due to the oxygen loss in the LSCF material at high temperatures without obvious change in F-containing gases. Hence, it can be confirmed here that the majority of F starts to leave the LSCF oxide lattice at a temperature as low as 700 °C mainly in the form of HF under air flow.

To further confirm the F loss measured by TGA-MS, an ex situ annealing measurement was also performed. A set of LSCFF0.20 powder samples were annealed at different temperatures, i.e., 700, 800, and 950 °C for a duration of 4 hours in a static ambient atmosphere and the fluorine concentration in the samples was determined via F-ion selective electrode measurements. After annealing at 700, 800, and 950 °C, the F stoichiometry in the annealed samples (initially 0.12(3)) drops to 0.06(2), 0.05(1), and ≈0.0001, respectively (Table S4 and Figure S10, Supporting Information). Thus, after calcination at 950 °C, the incorporated F ions in the anion sub-lattice can be considered as disappeared within the detection limit of the technique (electrode certified by the supplier for a minimum F^- concentration of 10^{-6}). Moreover, this F loss behavior can even be virtually observed with the colour change during the solution preparation for the F selective electrode measurements, as shown in (Figure S10, Supporting Information inset photo). The LSCF and LSCFF0.20-A after annealing at 950 °C both present a dark brown colour while the LSCFF0.20 before annealing presents a slightly light brown colour. This colour change also verifies that after calcination, the material chemistry of the LSCFF0.20-A powder is closer to the LSCF oxide material.

2.4. Modification in LSCFF0.2-A After Fluorine Loss Compared to Undoped LSCF

With the various techniques used for F determination, it can be confirmed that before the EIS measurements, the symmetric cells were all composed as: LSCF/CGO/YSZ. Then immediately comes the question: why the fluorine pre-treated LSCFF*x*-A symmetric cells still present lower R_p even without fluorine? In this section different characterisation techniques have been performed for LSCF and LSCFF0.20 samples after annealing: LSCF and LSCFF0.20 both annealed in the same temperatures as the symmetric cells (950 °C) for further investigation. These annealed samples are noted as LSCF-A and LSCFF0.20-A, respectively.

Firstly, pulsed isotopic exchange (PIE) experiments have been carried out up to 650 °C to investigate the oxygen surface exchange kinetics of four LSCFF*x* materials: LSCF oxide after 950 °C annealing: LSCF-A, as-prepared LSCFF0.05 powders, as-prepared LSCFF0.20 powders and LSCFF0.20 powders after 950 °C annealing: LSCFF0.2-A.

Figure 7 presents the Arrhenius plots of the corresponding overall exchange rate $\mathfrak{R}_0$ for the aforementioned four LSCFF*x* materials, as well as the dissociative adsorption and incorporation rates $\mathfrak{R}_a$ and $\mathfrak{R}_i$, which are calculated according to Equation (S5–S7, Supporting Information). The oxygen isotope fractions as a function of temperature for different samples are presented in Figure S11 (Supporting Information). The results indicate that under the applied conditions in PIE, $\mathfrak{R}_0$ presents a decreasing trend in the following order: annealed LSCF-A> as-prepared LSCFF0.05≈annealed LSCFF0.20-A > as-prepared LSCFF0.20. To emphasise again here, the as-prepared LSCFF0.05 and LSCFF0.20 are F-incorporated oxyfluoride materials while the annealed LSCFF0.20-A material is actually LSCF oxide material where the incorporated F ions have been replaced by oxygen ions or oxygen vacancies in the anionic sublattice. At 500 °C, the overall surface exchange rate $\mathfrak{R}_0$ of LSCF-A oxide is about two orders of magnitude higher than that of the F-incorporated LSCFF0.20 materials and is almost one order of magnitude higher than that of the LSCFF0.05 oxyfluoride powders. It is shown that with more F doping in the oxide lattice, the oxygen surface exchange rate is surprisingly decreasing, and after annealing (removing F) the oxygen surface exchange rate of LSCFF0.20-A is higher than that of LSCFF0.20. This suggests the F incorporation in LSCF oxide is potentially detrimental to the oxygen surface exchange kinetics. Additionally, the LSCFF0.20-A sample presents a lower oxygen surface exchange rate

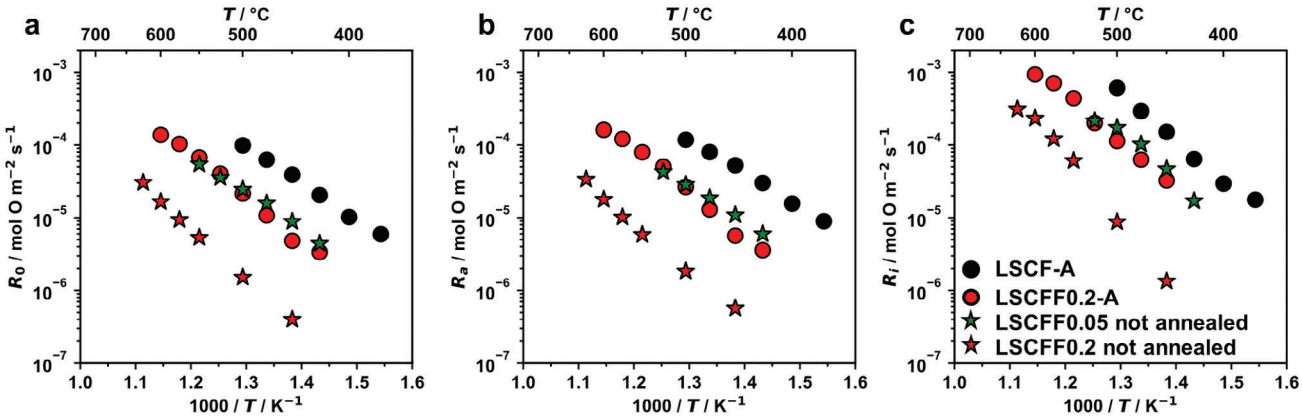

Figure 7. Arrhenius plots of $\mathfrak{R}_0$, $\mathfrak{R}_a$, and $\mathfrak{R}_i$ obtained via pulsed isotopic exchange measurements for LSCF-A and LSCFF0.20-A powders after annealing at 950 °C and the as-synthesised LSCFF0.05 and LSCFF0.2 powders without annealing.

compared with the LSCF-A oxide material and the reason for this remains unclear. The EIS results suggested that oxygen surface exchange and/or bulk diffusion were increased in the LSCFF*x*-A electrodes. The discrepancy found in the analysis of the EIS and PIE results could be explained by i) the improvement of the oxygen bulk diffusion and/or electronic conductivity only in the LSCFF*x*-A materials which would have a positive effect on the EIS performance and /or ii) the effect of polarisation which is not taken into account in the PIE results and which will be the objective of future work.

Moreover, for the PIE measurement, a two-step oxygen exchange model[49] was applied in which the processes of oxygen exchange into the oxide lattice are divided into two summed steps: step1-dissociative adsorption where the oxygen molecular bond is ruptured and isotopologues are redistributed; step2-incorporation process where oxygen ions cross the gas-solid interface. If the incorporation process is the rate-limiting step ($\mathfrak{R}_i < \mathfrak{R}_a$), the dissociated oxygen ions are more readily to form the $^{16}O^{18}O$ molecules on the powder surface instead of crossing the interface. From Figure 7b,c, it can be concluded that for all four LSCFF*x* materials tested in this work, the oxygen surface exchange is predominately limited by the dissociative adsorption process as $\mathfrak{R}_i > \mathfrak{R}_a$.

Figure S12 (Supporting Information) presents the high-quality XRD patterns of both annealed samples: LSCF-A and LSCFF0.20-A. Lattice parameters were determined after Rietveld refinement, and are very similar between samples within error: $a = 5.4911(5)$ Å, $c = 13.440(3)$ Å for LSCF-A, and $a = 5.4976(4)$ Å, $c = 13.436(2)$ Å for LSCFF0.20-A. This highlights that the overall transition metal oxidation state is very close in both samples at room temperature. Interestingly, within the limitation of lab X-ray, a difference in the peak shape can be clearly observed, with LSCFF0.20-A having a larger peak width than LSCF-A, which could be the result from stronger disorder in the former sample. In the future studies high-resolution synchrotron-based X-ray diffraction is still needed in order to obtain more structural information.

In addition, room temperature ^{57}Fe Mössbauer measurements have revealed different behavior of iron in the LSCF-A and LSCFF0.20-A samples (**Figure 8** and **Table 1**). LSCF-A can be described as the sum of one quadrupole doublet and one singlet, with isomer shifts of 0.26(3) and 0.06(1) mm s^{-1}, respectively. The former can be ascribed to mixed valence $Fe^{3+/4+}$, with electron hopping, in octahedral site, due to the lower isomer shift value compared to typical 6-fold coordinated Fe^{3+} in oxides (0.35 mm s^{-1}). The singlet can be ascribed to a Fe^{4+} as expected from the literature,[20,50] which accounts for ≈30% of the total resonant area. In LSCFF0.20-A, these two contributions are

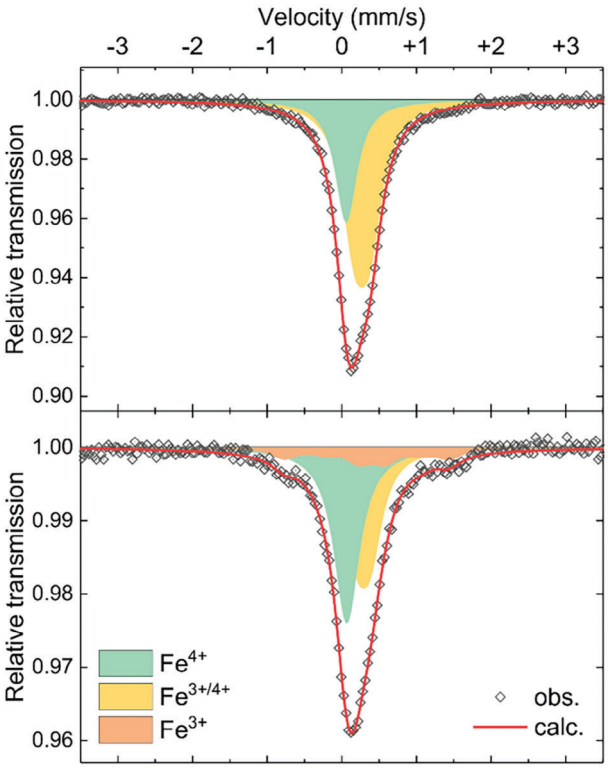

Figure 8. Room temperature (293 K) ^{57}Fe Mössbauer spectra on the LSCF-A powder(above) and LSCFF0.20-A powder (below) after annealing at 950 °C for 2 h.

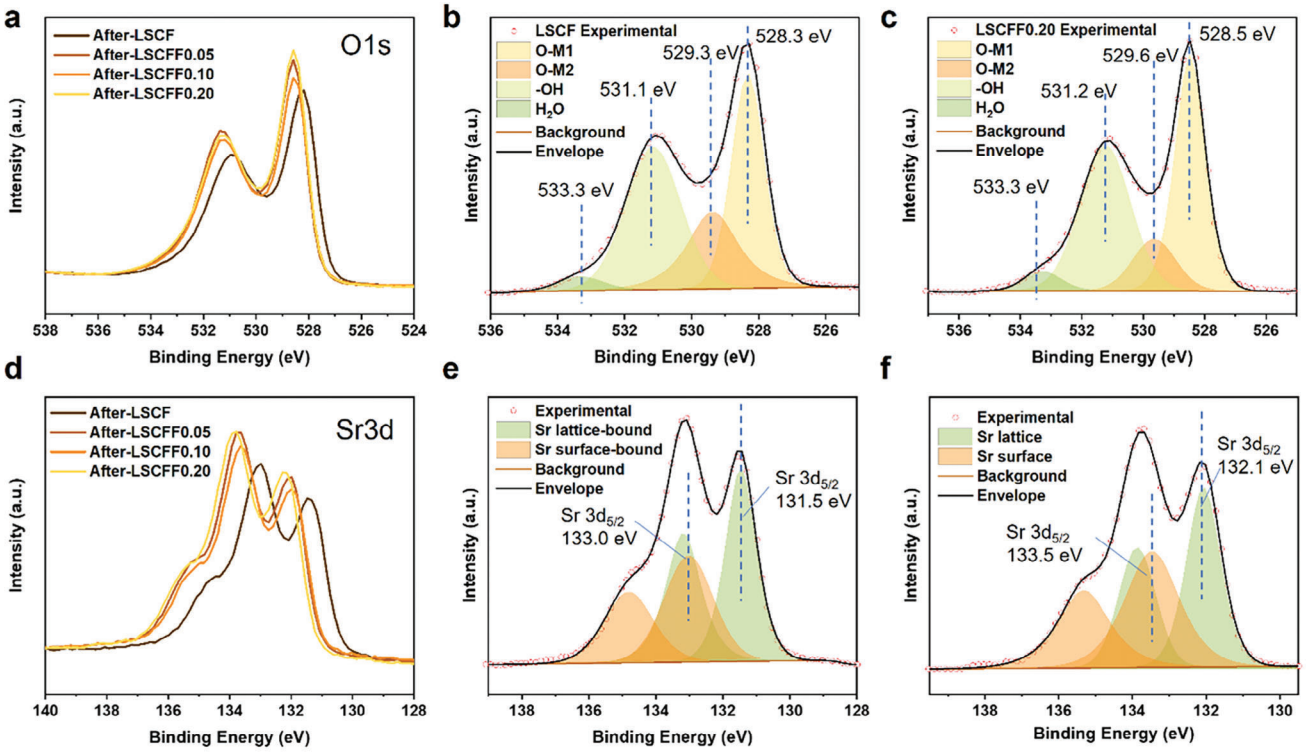

Figure 9. XPS a–c) O1s d–f) Sr3d spectra of the as-screen printed symmetric cells after high-temperature calcination.

also visible, and a third environment can be distinguished. This last component (sextet) with an isomer shift of 0.37 mm s^{-1} and hyperfine magnetic field (B_{hf}) of ≈7 T is associated with a not fully-ordered magnetic structure involving Fe^{3+} ions. Indeed, it has been shown by Berry et al.[20] that $La_{1-x}Sr_xFeO_{3-\delta}$ is paramagnetic at room temperature, while fluorination of the phases leads to considerable increase in the Néel temperature, bringing Fe^{3+} ions to interact anti-ferromagnetically at room temperature and above. One should have to mention that $LaFeO_3$ (100% Fe^{3+}) presents a canted antiferromagnetic ordering (T_N = 520–570 K).[51] This increase in the magnetic ordering temperature is ascribed to the increased amount of Fe^{3+} in the materials. Although temperature-dependant measurements are still needed to determine the Néel temperature in both LSCF-A and LSCFF0.20-A samples, it appears that the magnetic ordering temperature of Fe^{3+} ions increases in the later. This can be explained either by enhanced structural disorder or by the increased amount of Fe^{3+} vs. Fe^{4+}, thereby resulting in an increased amount of Co^{4+} in order to maintain a similar overall oxidation state in LSCFF0.20-A compared to LSCF-A (as has been observed by XRD analysis).

The change in Fe vs. Co oxidation states, and particularly the increased amount of Co^{4+} is another hypothesis for the improved electrochemical performances of LSCFF0.20-A, as this high valent cation is known for its high activity towards the OER process.[52,53] Further Mössbauer measurement at low temperature, as well as magnetic properties investigation, will be the object of future work to further confirm this result and obtain quantitative information on Fe and Co oxidation states.

Additionally, we examined more closely the XPS spectra on the aforementioned set of LSCFF*x*-A symmetric cells. Interestingly, the O1s (**Figure 9a**) and Sr 3d (Figure 9d) spectra of the LSCFF*x*-A samples are all shifted to higher binding energy compared to the LSCF-A sample while the core level of La 3d, Co 2p, and Fe 2p does not present significant changes with only subtle variations (Figure S13, Supporting Information) under the detection limit of XPS. The deconvolution images of the O 1s and Sr 3d spectra for LSCF-A and LSCFF0.20-A samples have been presented in Figure 9b,c and Figure 9e,f, respectively. The details of Sr 3d deconvolution for all samples are listed in Table S5 (Supporting Information). For all LSCFF*x*-A samples, two chemically different Sr-related species can be observed and labelled as two doublets with different colours. Unlike the as-prepared LSCFF*x* powder samples presented in Figure 2 where the energy separation for the two Sr 3d doublets is ca. 2.0 eV due to the higher binding energy of Sr—F bond, after calcination, the energy separation for the two doublets of Sr 3d is ca. 1.5 eV for all samples. Here the low binding energy component is attributed

Table 1. ^{57}Fe Mössbauer hyperfine parameters (293K) for samples after annealing at 950 °C for 2 h.

		δ [mm s^{-1}]	Δ or 2ε [mm s^{-1}]	B_{hf} (T)	Γ [mm s^{-1}]	Area (%)
LSCF-A	Fe^{4+}	0.06(1)	–	–	0.36(2)	30(3)
	$Fe^{3+/4+}$	0.26(3)	0.21(3)	–	0.41(2)	70(3)
LSCFF0.20-A	Fe^{4+}	0.07(2)	–	–	0.42(4)	45(3)
	$Fe^{3+/4+}$	0.28(3)	0.20(3)	–	0.38(5)	41(3)
	Fe^{3+}	0.37(4)	−0.07(5)	6.9(4)	0.40(5)	14(3)

to a Sr-bulk bond and a high binding energy component is attributed to a Sr surface species, such as $Sr(OH)_2$, SrO_x in good agreement with the literature.[35,38] Compared with the LSCF-A sample, the Sr 3d binding energy of the LSCFF*x*-A samples has positively shifted by 0.6 and 0.5 eV for the Sr lattice bond and Sr surface bond, respectively. Similarly, the O—metal bond of the LSCFFx-A samples has also positively shifted by 0.2–0.3 eV. This chemical shift for both O 1s and Sr 3d core level can unlikely be simply explained as an oxidation state change for oxygen and the alkaline earth element Sr. Instead, to be emphasised here, the binding energy measured via XPS represents the energy difference between the Fermi level of the sample and an occupied core level. For the LSCF oxide materials, although at high temperatures it presents a metallic behavior, at lower temperatures (<600 °C) a behavior of semi-conductor was reported.[54,55] Thus, at room temperature where the XPS was measured, for the LSCF with the semiconducting behavior, the Fermi level sits within the band gap and the band-referenced Fermi level can be significantly shifted due to small variation in oxygen stoichiometry.[56]

For the LSCFF*x* materials, after annealing at high temperature and with the presence of moisture, via exchanging with oxygen in one water molecule, two fluorine ions leave the lattice in the form of HF with one site occupied by water oxygen. The other F occupied site can either be compensated by forming oxygen vacancies (Equation (1), or compensated by a dissociated and incorporated oxygen from oxygen gas while the charge neutrality is balanced by the oxidation of transition metals such as Fe and Co (Equation 2):

$$2F_O^{\cdot} + H_2O \rightarrow 2HF + O_O^{\times} + V_O^{\cdot\cdot} \quad (1)$$

$$2F_O^{\cdot} + H_2O + 2Fe_{Co/Fe}^{'} + \frac{1}{2}O_2 \rightarrow 2HF + 2O_O^{\times} + 2Fe_{Co/Fe}^{\times} \quad (2)$$

$$2F_O^{\cdot} + H_2O + 2Co_{Co/Fe}^{'} + \frac{1}{2}O_2 \rightarrow 2HF + 2O_O^{\times} + 2Co_{Co/Fe}^{\times} \quad (3)$$

Considering Equation (1), since in the perovskite-structured materials, the oxygen diffusion is through oxygen vacancies, which is here suggested by room temperature XPS, an increased vacancy concentration is advantageous for oxygen transport. The preferential incorporation of fluorine in the vicinity of Sr^{2+}, observed by XPS, leading after annealing (HF departure) to the formation of oxygen vacancies contributes to enhancing the oxygen mobility around Fe^{3+}/Sr^{2+} connected cations. Also, during fluorination, the material reduces and forms a higher amount of Fe^{3+} than in the oxide parent phase. During annealing at high temperatures, vacancies are formed in the perovskite structure, while re-oxidation occurs in the originally fluorinated material (Equations 1 and 2). Consequently, the improvement in electronic conductivity after the loss of fluorine is probably due to greater oxidation of Co^{3+} ions into Co^{4+} linked to the stabilisation of holes in the t_{2g} orbitals.

Moreover, the distorted structure confirmed by XRD spectroscopy could potentially be beneficial for oxygen vacancy formation and diffusion at higher temperatures, with a decreased energy barrier. This is to say oxygen may be more prone to leave the lattice at a lower temperature and to diffuse, which further explains the performance enhancement is even better at a lower temperature, at 500 °C where oxygen surface exchange and diffusion contribute significantly to the total R_p. Additionally, at higher temperatures ≥ 750 °C, for the symmetric cells with LSCF and LSCFF*x* electrodes the contribution from oxygen diffusion in the electrodes is much less significant on the total polarisation resistance. Instead, the contributions are mainly from charge transfer and gas diffusion, and thus, the difference between different samples at high temperatures becomes negligible.

Therefore, through XRD, XPS and Mössbauer measurement analysis, we have raised several hypotheses to explain the improved electrochemical performances of the LSCFF*x*-A samples: 1) increased structural disorder, 2) increased oxygen vacancy concentration and 3) changes in the Co vs. Fe oxidation state, with higher Co^{4+} content in the formerly fluorinated phases. All these effects could be combined in various degrees and are susceptible to play a strong role in the oxygen anion diffusion, electronic conductivity and OER activity of the materials.

To summarise here, different from many literature reports, we demonstrate that the improved electrochemical performance in the LSCFFx symmetric cell is not because of the direct presence of fluorine, instead it is potentially due to the effect of fluorine loss on the crystallographic structure, electronic configuration and oxygen stoichiometry on the pristine material. However, further studies, such as magnetic, electronic/ionic transport measurements as well as the determination of oxygen vacancies as a function of temperature combined with computational simulation are still required for a deeper understanding of the changes at stake.

3. Conclusion

In this work, three LSCFF*x* (x = 0.05, 0.10, and 0.20) oxyfluoride materials have been prepared via low-temperature solid-state route with the polymer binder PVDF. Increased electrochemical performance with reduced ASR has been clearly observed for the ″LSCFF*x*″ symmetric cells which is in good agreement with the literature. Albeit many reports in literature ascribe this improved electrochemical performance to fluorine incorporation, with various chemical analysis a complete F loss has been confirmed for the 'LSCFF*x*' symmetric cells after high-temperature calcination for cell preparation. Moreover, surprisingly, the direct presence of F is actually proven to be disadvantageous for the oxygen surface exchange process via the pulsed isotopic exchange measurements. Combined with XPS and DRT analysis, one plausible explanation for the reduced ASR of the symmetric cell is the increased oxygen under-stoichiometry, i.e., increased oxygen vacancies. Other reasons are a more distorted structure, confirmed by XRD measurements, which can possibly assist oxygen vacancy formation at higher temperatures and oxygen diffusion in the bulk, or increased Co^{4+}/Fe^{4+} ratio, as suggested by Mössbauer spectroscopy. Further mechanism studies are certainly still required to confirm, to refute these hypotheses or to unfold the hidden possibilities and to understand whether the improved performance is able to be maintained with the presence of other gases. Meanwhile, questions whether the oxyfluoride materials are truly good candidates for devices operating at high temperatures remain to be answered. This work suggests that one must exercise due care in discussing about oxyfluoride materials or F-doped

oxides, especially for materials after thermal annealing at high temperatures, due to the possible fluorine loss. Meanwhile, it also indicates that a topochemical reaction with PVDF prior to cell calcination, can serve as a good strategy to engineer oxygen vacancies, structure distortion and electronic structure, which further improves the electrochemical performance of the oxide materials.

4. Experimental Section

Material Preparation: Three F-doped $La_{0.6}Sr_{0.4}Co_{0.2}Fe_{0.8}O_{3-x-\delta}F_x$ (LSCFF*x*) powders, x = 0.05 (LSCFF0.05), 0.10 (LSCFF0.10) and 0.20 (LSCFF0.20) were prepared via low temperature fluorination of $La_{0.6}Sr_{0.4}Co_{0.2}Fe_{0.8}O_{3-\delta}$ (LSCF6428, Marion Technologies) with poly(vinylidene fluoride) (PVDF), -$(C_2H_2F_2)_n$-. The powder precursor LSCF6428 oxide was first calcined at 850 °C for 3 h to remove the impurities before mixing with the PVDF binder. The solid powders of LSCF and PVDF were weighted stoichiometrically and mixed with mortar and pestle for 30 min. The mixed powders were then pressed into pellets by uniaxial pressing and annealed at 400 °C for a duration of 24 h with a heating and cooling rate of 5 °C min^{-1} under ambient atmosphere. To avoid cross-contamination, the pressed pellets were placed on top of the same powder bed and covered with the same powder mixture.

Characterization: The crystalline structure of each sample was recorded by lab X-ray diffraction (XRD) using Cu Kα radiation (λ = 1.5418 Å) in the 2θ range of 10–80° with a step size of 0.034°. The single-phase nature and the lattice parameters of the materials were determined via Le Bail and Rietveld refinements using the FullProf software suite.[57,58] For the Rietveld refinement analysis of LSCFF0.2-A and LSCF-A materials after high-temperature annealing, XRD data were collected on a PANalytical X'pert PRO MPD in Bragg–Brentano θ–2θ geometry equipped with a Ge (111) primary monochromator and X'Celerator multi-strip detector.

The cation composition of the commercial LSCF6428 was confirmed via the inductively coupled plasma (ICP) technique and the fluorine content of the oxyfluoride powders was measured by the ion-sensitive electrode technique. The details for the F-selective electrode measurements are provided in the Section S0.1 (Supporting Information).

The thermal stability of the LSCFF powders were examined via Thermogravimetric Analysis coupled with a mass spectrometer (TGA-MS). TGA-MS measurements were performed with a TG Setsys "Evo" apparatus from Setaram Instrumentation coupled on-line to a MS Thermo Quadstar massspectrometer (corrosive gas version). In all experiments, the carrier gas used was pure synthetic air (Air Liquide–Alphagaz 1, with a purity of: H_2O < 5 vpm, CO_2 < 0.5 vpm and total hydrocarbon (C_xH_y) < 0.1 vpm) at a flow of 100 mL min^{-1}. Heating was carried out at a rate of 5 K min^{-1} up to 1273 K and a platinum crucible was used as a sample holder. Decomposition gasses were passed through a temperature gas transfer line equipped with a stainless steel capillary. Both, the outlet of the TG apparatus and the gas transfer line are maintained at a constant temperature of 423 K to avoid cold heat sinks and thus to prevent the condensation of evolved gases.

Scanning electron microscopy (SEM) was applied to study the microstructure of the as-printed symmetric cells using a Jeol JSM 6700F microscope after metallizing the powders with gold, and further chemical element analysis was performed with the energy dispersive spectroscopy (EDX) detector (Si—Li), voltage of 15 kV and working distance of 10 mm.

X-ray Photoelectron Spectroscopy (XPS) measurements were carried out on a Thermo Fisher K-Alpha spectrometer with a monochromatic micro-focused Al Kα source (1486.71 eV) on both the as-prepared sample surface and after ion etching. The sputtering was performed with 3 keV argon ion beam with an EX06 Argon ION source.

A dual-beam time-of-flight secondary ion mass spectrometry (ToF-SIMS^5, IONTOF GmbH, Münster, Germany) analysis was performed with a 30 keV Bi^+ analysis beam and a 2 keV Cs^+ sputtering beam over an analysis area of 300 µm × 300 µm and a sputtering area of 500 µm × 500 µm.

Mössbauer experiments were performed in transmission geometry with a constant acceleration (Halder-type) spectrometer equipped with a ^{57}Co(Rh) radioactive source (nominal activity: 1.85 GBq) at room temperature. ^{57}Fe Mössbauer spectra of thin absorbers containing ≈5 mg cm^{-2} of iron were recorded at room temperature (293 K) and the hyperfine parameters (δ isomer shift, Δ quadrupole splitting, 2ε quadrupole shift, B_{hf} hyperfine magnetic field, Γ Lorentzian linewidth) and relative area of each component were refined using the WinNormos software (Wissenschaftliche Elektronik GmbH). Isomer shift values were relative to α-Fe^0 at room temperature.

Symmetric Cell Preparation and Electrochemical Measurements: Terpineol-based inks were first prepared using the LSCF and LSCFF*x* phases as the active materials for oxygen electrodes and 20% Gd-doped ceria (CGO20) for the interlayer. In order to achieve a good homogeneity and dispersion of the powders as well as decreased particle sizes, a process using a three-cylinder was also applied. The symmetric cells were then fabricated with the configuration of LSCFF*x*/CGO20/3% yittria-stabilised zirconia (3YSZ) electrolyte by the screen-printing technique. The CGO interlayer (φ = 16 mm) was first printed on both sides of the 3YSZ electrolyte (double side polished φ ≈ 20 mm) and the CGO layer was sintered at 1275 °C for 1 hr in an ambient atmosphere. Three/two LSCFF*x* electrode layers (φ = 14.5 mm, or φ = 16 mm for different sets) were then printed on top of the sintered CGO layers symmetrically and the printed cells were calcined at 950 °C for 4 h under ambient atmosphere. Before reaching the sintering temperature, the cells were held at 600 °C for one hour to burn out the organics in the slurry and were further heated up to the calcination temperature with a heating rate of 2 °C min^{-1}.

Electrochemical Impedance Spectroscopy (EIS) measurements were performed with a ModuLab XM MTS (Solartron analytical) from 1MHz–0.1Hz with 50 mV AC amplitude under static air in the temperature range of 400–800 °C. The configuration of the set-up can be found somewhere else[59] and gold mesh was used at the current collectors. The symmetric cells were first heated up to 800 °C with a heating rate of 5 °C min^{-1} and held at 800 °C overnight (>16 h). The measurements were carried out every 50 °C when the cells were thermally equilibrated at the temperature (hold at the temperature for min. 0.5–1 h). For the ageing experiments, the symmetric cells were held at 700 °C for over 300 h and the data were recorded regularly. Zview2 (Scribner, LLC.) was applied to fit the obtained complex impedance diagrams. The distribution relaxation time (DRT) analysis was further performed by using Python-based *pyDRTtools*.[60,61] The regularisation parameter was set as 1×10^{-3}.

Pulsed Isotopic Exchange (PIE): Pulsed isotopic exchange (PIE) was applied for rapid determination of the oxygen surface exchange kinetics of the LSCFF*x* samples with and without fluorine incorporation. The details about this technique are well explained in the literature.[62,63] Prior to the measurements, the surface area of the powders was determined by the BET (Brunauer, Emmett and Teller) approach. The powders were then loaded in a quartz reactor and secured by quartz wool plugs on both sides. The measurements were carried out in the temperature range of 350–650 °C under a carrier gas of mixed Ar and O_2 with pO_2 = 200 mbar. Before reaching the power bed of the samples, the carrier gas was first dried by passing through a moisture filter (Agilent CP17971). The N_2 and $^{18}O_2$ pulse with pO_2 = 200 mbar was first introduced in a 500 µL loop and injected by switching a six-port valve. A schematic of the six-way valve has been provided in supplementary information Figure S1 (Supporting Information). An INFICON mass spectrometer (Transpector 2 Gas Analysis System) was connected at the outlet of the quartz reactor and continuously following the outlet gases. The details on the calculated overall surface exchange rate $\mathfrak{R}_0$ (mol m^{-2} s^{-1}), the dissociative and incorporation absorption rates $\mathfrak{R}_a$ and $\mathfrak{R}_i$ were provided in the Section S0.2 (Supporting Information).

Supporting Information

Supporting Information is available from the Wiley Online Library or from the author.

Acknowledgements

Z.S., J.M.B., and J.G. would like to acknowledge Regional Project CASTOR (Co-electrolysis ASisted by catalysis for electricity STORage), convention number: AAPR2021-2020-11813510 and Dr Christine Labrugère Sarroste and Dr Jean-Paul Salvetat for their help with the XPS and ToF-SIMS measurements. Z.S. wishes to thank HORIZON-MSCA-2021-PF-01, project no. 101064349 NATFOX. The authors thank Eric Lebrault from the ICMCB Diffraction Service for performing laboratory X-Ray diffraction scans and Sonia Buffière from ICMCB Mutual Services for the SEM imaging. Z.S., J.M.B., S.F., and J.G. would like to thank Prof. Henny J.M. Bouwmeester for fruitful discussions and help on the pulsed isotopic exchange technique.

Conflict of Interest

The authors declare no conflict of interest.

Author Contributions

This work was performed through contributions of all authors. J.G. and J.-M.B. directed the project. Z.S. and J.G. prepared the samples; All authors Z.S., J.G., J.-M.B., S.F., A.D., E.D., L.T.-G., and M.D. performed investigation. Z.S. and J.G. wrote the original draft; All authors reviewed and edited the final manuscript.

Data availability Statement

The data that support the findings of this study are available from the corresponding author upon reasonable request.

Keywords

fluorine doping, LSCF, mixed anions, polarization resistance, solid oxide cell

Received: April 4, 2024
Revised: May 7, 2024
Published online:

[1] D. Guan, B. Wang, J. Zhang, R. Shi, K. Jiao, L. Li, Y. Wang, B. Xie, Q. Zhang, J. Yu, Y. Zhu, Z. Shao, M. Ni, *Energy Environ. Sci.* **2023**, *16*, 4926.
[2] A. Hauch, R. Küngas, P. Blennow, A. B. Hansen, J. B. Hansen, B. V. Mathiesen, M. B. Mogensen, *Science* **2020**, *370*, 6118.
[3] J. K. Harada, N. Charles, K. R. Poeppelmeier, J. M. Rondinelli, *Adv. Mater.* **2019**, *31*, 1805295.
[4] R. D. Shannon, *Acta Crystallogr. A* **1976**, *32*, 751.
[5] K. Funke, R. D. Banhatti, *Solid State Ionics* **2006**, *177*, 1551.
[6] Z. Zhang, Y. Zhu, Y. Zhong, W. Zhou, Z. Shao, *Adv. Energy Mater.* **2017**, *7*, 1700242.
[7] C. Yang, A. Grimaud, *Catalysts* **2017**, *7*, 149.
[8] P. R. Slater, P. Edwards, C. Greaves, I. Gameson, M. G. Francesconi, J. P. Hodges, M. A1-Mamouri, M. Slaski, *Phys. C* **1995**, *241*, 151.
[9] P. R. Slater, K. B. Gover, *J. Mater. Chem.* **2001**, *11*, 2035.
[10] G. Li, Y. Gou, R. Ren, C. Xu, J. Qiao, W. Sun, Z. Wang, K. Sun, *J. Power Sources* **2021**, *508*, 230343.
[11] P. Lightfoot, S. Pei, J. D. Jorgrnsen, X.-X. Tang, A. Manthiram, J. B. Goodenough, *Phys. C* **1990**, *169*, 15.
[12] J. Zhu, G. Liu, Z. Liu, Z. Chu, W. Jin, N. Xu, *Adv. Mater.* **2016**, *28*, 3511.
[13] A. P. Tarutin, G. K. Vdovin, D. A. Medvedev, A. A. Yaremchenko, *Electrochim. Acta* **2020**, *337*, 135808.
[14] J. Gamon, J. M. Bassat, A. Villesuzanne, M. Duttine, M. Batuk, D. Vandemeulebroucke, J. Hadermann, F. Alassani, F. Weill, E. Durand, A. Demourgues, *Inorg. Chem.* **2023**, *62*, 10822.
[15] A. M. Abakumov, J. Hadermann, G. Van Tendeloo, R. V. Shpanchenko, P. N. Oleinikov, E. V. Antipov, *J. Solid State Chem.* **1999**, *142*, 440.
[16] M. Al-Mamouri, P. P. Edwards, C. Greaves, P. R. Slater, M. Slaskib, *J. Mater. Chem.* **1995**, *5*, 913.
[17] P. R. Slater, *J. Fluorine Chem.* **2002**, *117*, 43.
[18] J. Jacobs, M. A. L. Marques, H. C. Wang, E. Dieterich, S. G. Ebbinghaus, *Inorg. Chem.* **2021**, *60*, 13646.
[19] O. Clemens, M. Kuhn, R. Haberkorn, *J. Solid State Chem.* **2011**, *184*, 2870.
[20] F. J. Berry, X. Ren, R. Heap, P. Slater, M. F. Thomas, *J. Phys. Chem. Solids* **2008**, *69*, 2032.
[21] O. Clemens, R. Haberkorn, P. R. Slater, H. P. Beck, *Solid State Sci.* **2010**, *12*, 1455.
[22] N. Hou, J. Gan, Q. Yan, Y. Zhao, Y. Li, *J. Power Sources* **2022**, *521*, 230932.
[23] R. Guan, Z. Wang, H. Xu, X. Hao, L. Yang, J. Liu, S. Yu, T. He, *ACS Appl. Energy Mater.* **2022**, *5*, 481.
[24] H. Li, Z. Lü, *Int. J. Hydrogen Energy* **2021**, *46*, 2503.
[25] L. Zhang, W. Sun, C. Xu, R. Ren, X. Yang, J. Qiao, Z. Wang, K. Sun, *J. Mater. Chem. A* **2020**, *8*, 14091.
[26] K. T. Jacob, V. S. Saji, Y. Waseda, *Int. J. Appl. Ceram. Technol.* **2006**, *3*, 312.
[27] M. Sturza, S. Daviero-Minaud, H. Kabbour, O. Gardoll, O. Mentré, *Chem. Mater.* **2010**, *22*, 6726.
[28] J. Jacobs, J. R. Hester, S. G. Ebbinghaus, *Inorg. Chem.* **2022**, *61*, 17202.
[29] D. A. Osinkin, D. M. Zakharov, A. V. Khodimchuk, E. P. Antonova, N. M. Bogdanovich, E. V. Gordeev, A. Y. Suntsov, N. M. Porotnikova, *Int. J. Hydrogen Energy* **2023**, *48*, 22624.
[30] K. Wissel, J. Heldt, P. B. Groszewicz, S. Dasgupta, H. Breitzke, M. Donzelli, A. I. Waidha, A. D. Fortes, J. Rohrer, P. R. Slater, G. Buntkowsky, O. Clemens, *Inorg. Chem.* **2018**, *57*, 6549.
[31] Y. Xie, N. Shi, D. Huan, W. Tan, J. Zhu, X. Zheng, H. Pan, R. Peng, C. Xia, *ChemSusChem* **2018**, *11*, 3423.
[32] J. Xiong, H. Zhong, J. Li, X. Zhang, J. Shi, W. Cai, K. Qu, C. Zhu, Z. Yang, S. P. Beckman, H. Cheng, *Appl. Catal., B* **2019**, *256*, 117817.
[33] Y. Liu, X. Meng, F. Yu, M. Yin, N. Yang, B. Meng, M. V. Sofianos, S. Liu, *Int. J. Hydrogen Energy* **2018**, *43*, 12328.
[34] J. F. Moulder, W. F. Stickle, P. E. Sobol, K. D. Bomben, J. Chastain, *Handbook of X-Ray Photoemission Spectroscopy*, Perkin-Elmer Corporation, Minnesota, **1992**.
[35] O. Celikbilek, A. Cavallaro, G. Kerherve, S. Fearn, O. Chaix-Pluchery, A. Aguadero, J. A. Kilner, S. J. Skinner, *ACS Appl. Mater. Interfaces* **2020**, *12*, 34388.
[36] H. Idriss, *Surf. Sci.* **2021**, *712*, 121894.
[37] A. Nenning, E. Navickas, H. Hutter, J. Fleig, *J. Phys. Chem. Lett.* **2016**, *7*, 2826.
[38] Z. Sha, Z. Shen, E. Calì, J. A. Kilner, S. J. Skinner, *J. Mater. Chem. A* **2023**, *11*, 5645.
[39] S. B. Adler, J. A. Lane, B. C. H. Steele, *J. Electrochem. Soc.* **1996**, *143*, 3554.
[40] M. Schönleber, D. Klotz, E. Ivers-Tiffée, *Electrochim. Acta* **2014**, *131*, 20.
[41] D. Pérez-Coll, A. Aguadero, M. J. Escudero, L. Daza, *J. Power Sources* **2009**, *192*, 2.
[42] M. J. Jørgensen, M. Mogensen, *J. Electrochem. Soc.* **2001**, *148*, A433.
[43] F. Mauvy, C. Lalanne, J.-M. Bassat, J.-C. Grenier, H. Zhao, L. Huo, P. Stevens, *J. Electrochem. Soc.* **2006**, *153*, A1547.

[44] C. Nicollet, A. Flura, V. Vibhu, A. Rougier, J. M. Bassat, J. C. Grenier, *J. Power Sources* **2015**, *294*, 473.
[45] G. DiGiuseppe, A. Hunter, F. Zhu, *Electrochim. Acta* **2020**, *350*, 136252.
[46] Z. Xie, I. Jang, M. Ouyang, A. Hankin, S. J. Skinner, *J. Phys. Energy* **2023**, *5*, 045005.
[47] N. Tarasova, M. B. Hanif, N. K. Janjua, S. Anwar, M. Motola, D. Medvedev, *Int. J. Hydrogen Energy* **2024**, *50*, 104.
[48] Z. Shen, J. Wu, M. Shorvon, G. Cazaux, S. Parker, S. Skinner, *Chem. Mater.* **2021**, *33*, 4045.
[49] M. W. Den Otter, B. A. Boukamp, H. J. M. Bouwmeester, *Solid State Ionics* **2001**, *139*, 89.
[50] A. Mahmoud, M. Al Daroukh, M. Lipinska-Chwalek, M. Luysberg, F. Tietz, R. P. Hermann, *Solid State Ionics* **2017**, *312*, 38.
[51] P. V. Coutinho, F. Cunha, P. Barrozo, *Solid State Commun.* **2017**, *252*, 59.
[52] A. Moysiadou, S. Lee, C. S. Hsu, H. M. Chen, X. Hu, *J. Am. Chem. Soc.* **2020**, *142*, 11901.
[53] J. Zhou, L. Zhang, Y. C. Huang, C. L. Dong, H. J. Lin, C.-T. Chen, L. H. Tjeng, Z. Hu, *Nat. Commun.* **2020**, *11*, 378.
[54] A. Jun, S. Yoo, O. H. Gwon, J. Shin, G. Kim, *Electrochim. Acta* **2013**, *89*, 372.
[55] A. M. Ritzmann, J. M. Dieterich, E. A. Carter, *Phys. Chem. Chem. Phys.* **2016**, *18*, 12260.
[56] A. Nenning, A. K. Opitz, C. Rameshan, R. Rameshan, R. Blume, M. Hävecker, A. Knop-Gericke, G. Rupprechter, B. Klötzer, J. Fleig, *J. Phys. Chem. C* **2016**, *120*, 1461.
[57] T. Roisnel, J. Rodríguez-Carvaja, *Mater. Sci. Forum* **2001**, *118*.
[58] J. Rodríguez-Carvaja, *Newsletter* **2001**, *26*, 12.
[59] V. Vibhu, A. Flura, A. Rougier, C. Nicollet, S. Fourcade, T. Hungria, J. C. Grenier, J. M. Bassat, *J. Energy Chem.* **2020**, *46*, 62.
[60] T. H. Wan, M. Saccoccio, C. Chen, F. Ciucci, *Electrochim. Acta* **2015**, *184*, 483.
[61] A. Maradesa, B. Py, T. H. Wan, M. B. Effat, F. Ciucci, *J. Electrochem. Soc.* **2023**, *170*, 030502.
[62] H. J. M. Bouwmeester, C. Song, J. Zhu, J. Yi, M. Van Sint Annaland, B. A. Boukamp, *Phys. Chem. Chem. Phys.* **2009**, *11*, 9640.
[63] J. Song, *Correlating Structure and Oxygen Non-Stoichiometry with Transport Behaviour of Mixed Ionic-Electronic Conducting Perovskite-Related Oxides*, University of Twente, Enschede, Netherlands **2020**.